Journal of *Marine Science and Engineering*

MDPI

Article

Study of Velocity Changes Induced by *Posidonia oceanica* Surrogate and Sediment Transport Implications

Carlos Astudillo-Gutierrez [1,2,*], Iván Cáceres Rabionet [1,2], Vicente Gracia Garcia [1,2], Joan Pau Sierra Pedrico [1,2] and Agustín Sánchez-Arcilla Conejo [1,2]

[1] Laboratori d'Enginyeria Marítima, Universitat Politècnica de Catalunya, Jordi Girona 1-3, Mòdul D1, 08034 Barcelona, Spain; i.caceres@upc.edu (I.C.R.); vicente.gracia@upc.edu (V.G.G.); joan.pau.sierra@upc.edu (J.P.S.P.); agustin.arcilla@upc.edu (A.S.-A.C.)

[2] Centre Internacional d'Investigació dels Recursos Costaners (CIIRC), Jordi Girona 14-3, Mòdul D1, 08034 Barcelona, Spain

* Correspondence: carlos.astudillo@upc.edu

Abstract: An analysis of the interactions between wave-induced velocities and seagrass meadows has been conducted based on the large-scale CIEM wave flume data. Incident irregular wave trains act on an initial 1:15 sand beach profile with measurement stations from the offshore of a surrogate meadow until the outer breaking zone, after crossing the seagrass meadow. The analysis considers variability and peaks of velocities, together with their skewness and asymmetry, to determine the effects of the seagrass meadow on the near bed sediment transport. Velocity variability was characterized by the standard deviation, and the greatest changes were found in the area right behind the meadow. In this zone, the negative peak velocities decreased by up to 20.3%, and the positive peak velocities increased by up to 11.7%. For more onshore positions, the negative and positive peak velocities similarly decreased and increased in most of the studied stations. A progressive increase in skewness as the waves passed through the meadow, together with a slight decrease in asymmetry, was observed and associated with the meadow effect. Moving shoreward along the profile, the values of skewness and asymmetry increased progressively relative to the position of the main sandbar. The megaripple-like bedforms appeared earlier when the meadow was present due to the higher skewness, showing a belated development in the layout without the meadow, when skewness increased further offshore due to the proximity of the breaker sandbar. To assess the sediment transport capacity of a submerged meadow, the SANTOSS formula was applied, showing that in front of the meadow, there was a higher sediment transport capacity, whereas behind the meadow, that capacity could be reduced by up to 41.3%. In addition, this formula was able to produce a suitable estimate of sediment transport across the profile, although it could not properly estimate the sediment volumes associated with the bedforms generated in the profile.

Keywords: *Posidonia oceanica*; seagrass; wave-vegetation interactions; orbital velocity; asymmetry; skewness; sediment transport

Citation: Astudillo-Gutierrez, C.; Rabionet, I.C.; Garcia, V.G.; Pedrico, J.P.S.; Conejo, A.S.-A. Study of Velocity Changes Induced by *Posidonia oceanica* Surrogate and Sediment Transport Implications. *J. Mar. Sci. Eng.* **2024**, *12*, 569. https://doi.org/10.3390/jmse12040569

Academic Editor: Eugen Rusu

Received: 15 February 2024
Revised: 14 March 2024
Accepted: 21 March 2024
Published: 27 March 2024

1. Introduction

Coastal degradation has become a pressing problem due to changes in natural coastal conditions, mainly linked to population growth and an expanding global economy [1,2]. This degradation has been aggravated by climate change and rising sea levels, which have further deepened and accelerated this phenomenon [3,4]. As a result, coastal areas have been increasingly exposed to hazards such as erosion and flooding, which are expected to worsen in the coming years [5–9].

The solutions that have been proposed to address these problems have been totally dependent on traditional structures, such as seawalls, breakwaters, and other structures [10–14]. While these structures have solved specific problems of coastal protection

in the short (several years) and medium term (one decade), they have been incapable of addressing issues such as the sea level rise in the long term (several decades) [15,16]. The cost of maintaining these structures and, in some cases, of retrofitting them, is so high that it makes them unsustainable in the long term [17–20].

Given the problems caused by the rigidification of the coastline, more sustainable alternatives have been evaluated in recent years to ensure the long-term effectiveness of coastal protection [21–23]. A wide variety of marine ecosystems have been evaluated for their effectiveness against climate-change-related impacts, such as mean sea level rise [24,25], wave height variability [26–28], or coastal erosion [29,30]. This has generated complementary alternatives to the hard engineering interventions that have dominated the urbanized coastal landscape for years [31–33]. In addition, marine ecosystems have been able to deliver effective ecological [34,35] and economic value over time [34,36,37]. Seagrass meadows have been an example of how these ecosystems can provide protection from climate-change-related events [38,39], by reducing wave currents, in order to support a variety of species that enrich the marine ecosystem [40,41].

The role of seagrass in coastal protection has been evaluated in both field [42–44] and laboratory research [26,45,46]. In recent years, experimental research with surrogate materials that mimic seagrass meadows has increased [47–49], improving knowledge of the physical processes that govern the hydrodynamic changes produced by these ecosystems. However, studies have continued to focus on meadow zone processes, without monitoring the continuity of changes observed in onshore areas closer to the coastline [26,48–51].

Experiments with natural plants have proven difficult to replicate due to the complex interplay of factors in their natural habitat, such as variations in light, salinity, nutrients, or water quality, which can trigger stress responses and alter plant properties such as buoyancy or stiffness [52]. In addition, *Posidonia oceanica* meadows are protected from extraction from their natural habitat. Therefore, the use of surrogate materials is required to conduct large-scale experiments. To create an accurate mimic of *Posidonia oceanica*, a material was carefully selected to replicate the leaf behavior under wave action, as described by [47]. This involved considering materials with densities and yield strengths similar to those of the actual leaves, while ensuring that the dimensions closely matched those of the species.

The work presented here aims to evaluate the process of velocity changes produced by a surrogate *Posidonia oceanica* meadow in the nearest area behind the meadow. In addition, it assesses how these changes propagate along a beach profile up to the breaking location. Moreover, a sediment transport formula is used to corroborate the effect of velocity changes over the decrease in onshore sediment transport measured under the presence of the *Posidonia oceanica* meadow [47].

2. Materials and Methods

2.1. Experimental Setup

The present data were acquired during experiments conducted in the large-scale wave flume Canal d'Investigació i Experimentació Marítima (CIEM) of the Universitat Politècnica de Catalunya (UPC) in Barcelona, Spain (Figure 1b,c). The wave flume is 100 m long, 3 m wide, and 4.5 m deep. The horizontal coordinate X has the origin (X = 0 m) at the toe of the wave paddle in still water conditions and increases positively towards the beach. The vertical coordinate Z has the origin at the still water level (Z = 0 m) and is positive upwards and negative downwards. The flume contained a mobile sand bed with a slope of 1:15. The beach profile was made of commercial well-sorted sand, according to the method of moments [53], with a medium sediment size of d_{50} = 0.25 mm. The sediment density was 2650 kg m^{-3} with a porosity of loosely packed sand (P) equal to 0.4. The measured settling velocity (w_s) was equal to 0.034 ms^{-1}.

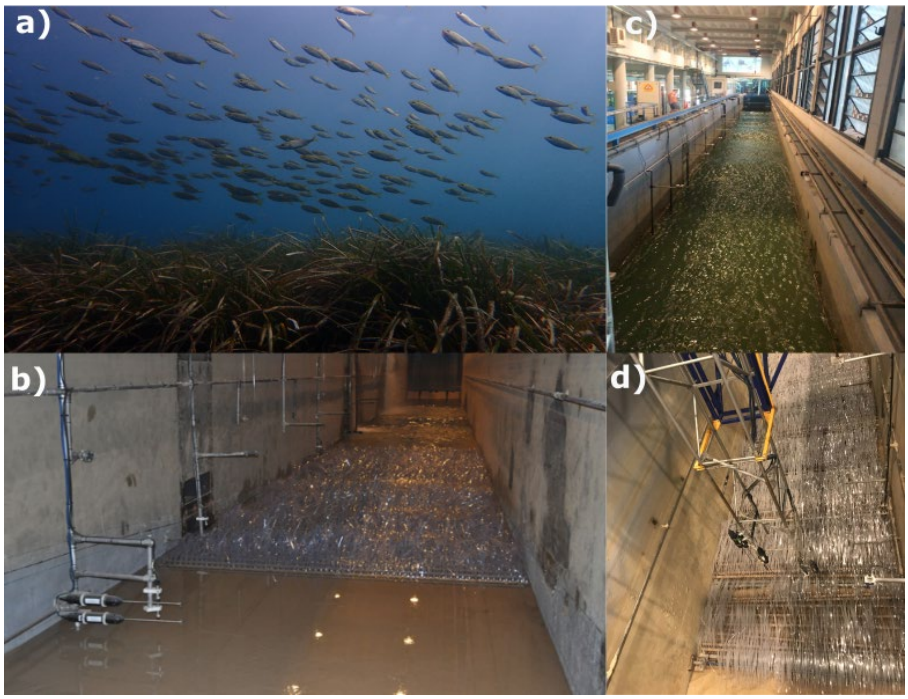

Figure 1. (**a**) *Posidonia oceanica* meadow located on the Mediterranean coast of Catalonia. (**b**) Surrogate *Posidonia oceanica* meadow arranged at the CIEM to carry out wave tests. (**c**) Start of experimental waves with surrogate seagrass meadow. (**d**) ADVs sensors on the mobile frame used to measure velocities at different positions on the profile.

A full-scale mimic of *Posidonia oceanica* was made with polyvinyl chloride (PVC), as detailed in Figure 1b,d. A single plant was constituted of 2 pairs of leaves 60 cm and 40 cm long each, with a leaf thickness of 0.5 mm. The leaves were inserted (stapled) into a wooden support (3.8 × 3.8 cm^2), simulating a rigid rhizome. The configuration of selected leaves, the materials used for the fabrication of the surrogate Posidonia and details of the construction of the meadow seagrass can be reviewed in [47]. The length of the meadows was selected to be 10 m long, maintaining the density of meadows of 269 units per m^2 and meadow width of 2.9 m. Special care was taken to ensure that these dimensions accurately reflect those of a real *Posidonia oceanica* seagrass meadow (Figure 1a). The flume water depth was 2.0 m at the wave paddle toe, generating a submergence ratio in the meadow area of 0.316. Previous studies [26,27,47] showed that submergence ratios around 0.3 can generate relevant wave height damping. From wave paddle up to X = 29 m, the bottom was flat, and no sediments were present. After this point, a 12 m flat sandy region was created with a thickness of 0.12 m. At X = 41 m, a constant handmade slope of 1:15 started and was built until the end of the flume. A mimic meadow was located from X = 30 m until X = 40 m (Figure 2).

Irregular waves with a significant wave height (H_s) value of 0.60 m and peak period (T_p) of 3.71 s were generated at the CIEM. The same wave conditions were tested for two layouts: A beach profile without seagrass (BR60) and a condition with seagrass meadows (R60). The irregular waves were composed of a series of 500 waves spanning a duration of 30 min (test), following a JONSWAP spectrum with gamma equal to 3.3. In total, for each layout, 12 tests were conducted, sequentially listed in time from t1 (first test) to t12 (final test). For our analysis, changes in wave profile and wave hydrodynamics were evaluated after and during each test, respectively.

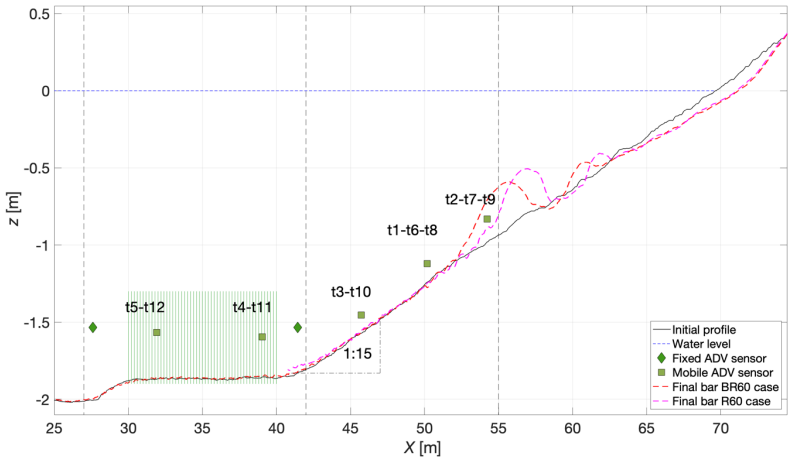

Figure 2. Cross-profile positioning of all sensors deployed in the BR60 and R60 layouts (see text for details). The small squares and small circles represent successive positions of mobile trolley stations, showing how all sensors are repositioned every 30 min after the end of each wave set. The meadow is represented by green vertical lines on the flat part of the flume.

Wave height variations in the meadow area were monitored by 4 pore pressure transducers (PPT), previously calibrated and positioned as detailed in Figure 2. The sand profile was measured after each test (every 30 min) with a mechanical profiler with an accuracy of ±1 cm [54]. Measurements of the profile evolution were taken at the central part of the flume. Velocity measurements were taken using vertical Nortek Vectrino acoustic Doppler velocimeters (ADVs). The ADVs used an acoustic frequency of 10 MHz and were configured to measure with a transmission length of 1.2 mm and a sampling volume of 4.9 mm. Two ADVs were fixed (green diamonds in Figure 2) in positions at the front and behind the meadow (X = 27.6 m and 41.4 m, respectively), and measured velocities during all tests (Figure 1b). Additionally, 4 ADVs were installed on a mobile frame at different elevations (with a distance of 0.51 m, 0.19 m, and 0.29 m between them, respectively) to measure the velocity profile along the flume (Figure 1c). For the analytical phase of this study, the ADV sensor positioned in closest proximity to the seabed was analyzed. To investigate various positions within the profile, the mobile frame was systematically relocated to distinct X and Z coordinates after the completion of each test, as detailed in Table 1 and green squares in Figure 2.

Table 1. Position of the ADV on the mobile frame, according to the tests conducted tests.

Position (m)	Tests Associated with the Position
X = 50.2	t1, t6 and t8
X = 54.2	t2, t7 and t9
X = 45.7	t3 and t10
X = 39.1	t4 and t11
X = 31.9	t5–t12

2.2. Data Analysis

From the three components of the collected velocity data (u, v, and w were relative to the X, Y, and Z axis, respectively), the analysis will focus on the u horizontal component presenting the velocities along the wave flume, representing the cross-shore velocity component on a beach. The u velocity can be broken down into three parts using the phase average technique (Equation (1)), like [55–58].

$$u = U_c + U_w + u' \quad (1)$$

The steady velocity (U_c) was associated with the current and was obtained with time-average velocity (Equation (2)), considering $u(\varphi)$ as the instantaneous velocity according to the φ phase [57]. The unsteady velocity (U_w) refers to oscillatory flows and was defined as the root mean square (RMS) of $u(\varphi)$ (Equation (3)), and u' represented the turbulent velocity fluctuation.

$$U_c = \frac{1}{2\pi}\int_0^{2\pi} u(\varphi)d\varphi \tag{2}$$

$$U_w = \sqrt{\frac{1}{2\pi}\int_0^{2\pi} (u(\varphi) - U_C)^2 d\varphi} \tag{3}$$

In order to measure the degree of linearity of velocity and the changes generated by the meadow effect, it was decided to assess the velocities skewness (Sk) and the asymmetry (As) defined by [59] in Equations (4) and (5), respectively,

$$Sk(x) = \frac{\overline{(u(x,t) - U_c)^3}}{U_w^3(x)} \tag{4}$$

$$As(x) = -\frac{\overline{\Im(\mathcal{H}(u))^3}}{U_w^3(x)} \tag{5}$$

where $u(x, t)$ is the cross-shore horizontal velocity, $\Im$ denoted the imaginary part of the Hilbert transform of instantaneous velocity, and the over-bar denoted time average for each test. Note that $Sk = 0$ denotes that crests and troughs have equal amplitudes, and $Sk > 0$ indicates that the amplitude of the crest is greater than that of the troughs. Furthermore, $As = 0$ denotes symmetry in the front and back faces of the wave. A wave becomes increasingly asymmetric as the crest travels faster than the troughs.

2.3. Data Processing

The data processing was carried out according to the diagram in Figure 3. All ADV time series were processed, and spike noise was eliminated using the method developed by [60]. The time interval between 0.5 and 25.5 min was considered, discarding the initial and final values of each series (Time series cutting). The velocity values were cleaned after considering the amplitude, signal-to-noise ratio, and correlation of the acquired signal. All values that presented an amplitude value lower than 75, a signal-to-noise ratio lower than 15 dB, and a correlation lower than 70% were discarded, and *NaN* values were inserted into those time series. In addition, velocity values that exceeded 4 times the standard deviation of the average for the series were eliminated following the works of [58,61].

After applying the filters, we worked with an average of 95.3% (BR60) and 92.0% (R60) of the total data for the original series among all sensors. The greatest removal of data occurred in test 1 and in the upper sensors of the mobile carriage, specifically in the area closest to the bar. After the data were despiked on the lower mobile trolley and fixed to sensors, 96% and 95.6% of the data were used in the analysis for the BR60 and R60 layouts, respectively.

The velocity analysis was carried out using two methods: graphical and numerical. The first analysis focused on identifying the discrepancies in each layout, taking into account the velocity variations at the same test number and sensor position. The numerical method focused on the changes in the measured velocities, considering the sensor variability equal to the standard deviation obtained from the compared velocity values. The velocity variability was obtained from two different approaches: one for the values of the whole series, and another for the peak values of the series (maxima or crest and minima or trough). The first method considers the mean value of the standard deviations of u at each time in the series. The second takes into account the maximum (positive) and minimum (negative) peak values of a wave cycle. For each peak at its time position, the standard deviation (variability) was computed and the mean value of these standard deviations was

calculated. Only the peaks that were perfectly located at the same time in the all-time series were considered, while the peaks that had some mismatch in time were discarded in order to reduce the errors that could appear when comparing velocity peaks from different waves.

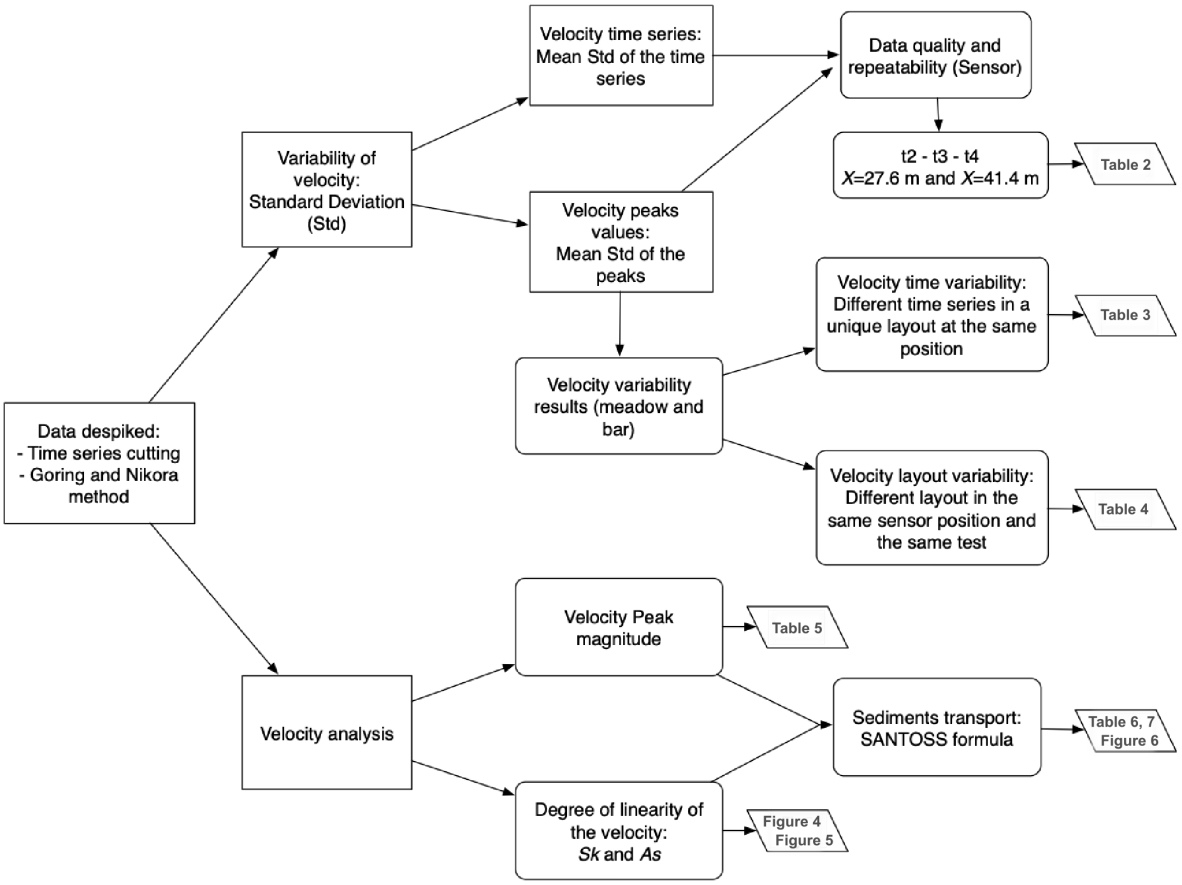

Figure 3. Block diagram representing the conceptual approach in this study, including velocity data processing from the ADV sensors and the derived results.

To ensure the accuracy of the experimentally collected velocity data, the quality and repeatability of the data were checked following both approaches (Table 2). Each method used the data acquired from the ADV located at 0.23 m from the bottom in front of and behind the meadow (X = 27.6 m and X = 41.4 m, respectively). The comparison of the velocity data was made between t2, t3, and t4 tests for the BR60 and R60 layouts. Test 1 has been discarded from this analysis as it is the first test after manual reshaping where the suspended sediment may be higher, thus generating a poor-quality ADV signal. The effect of the growing bar at t2, t3, and t4 (with a maximum height of 0.13 m and 0.14 m, located at X = 58.6 m and X = 59.6 m for BR60 and R60, respectively) is negligible at this early stage, so that both layouts should be mainly affected by the presence or absence of the meadow.

Table 2. Illustration of data variability for the (t2–t3–t4) time series, with the peaks for each studied layout.

Position (m)	Case	Series Variability (ms^{-1})	Peaks (+) Variability (ms^{-1})	Peaks (−) Variability (ms^{-1})
X = 27.6	BR60		0.017	0.009
X = 27.6	R60	0.013	0.009	0.010
X = 41.4	BR60	0.018	0.018	0.016
X = 41.4	R60	0.027	0.013	0.017

From the results obtained in Table 2, it can be seen that the variabilities between the series and peak values are similar, including the variability of positive (+) and negative (−) peaks. In addition, the variability values are slightly higher at later positions of the meadows, which may be related to the beginning of the slope zone at X = 41.1 m.

To assess the variability of velocities due to meadow and bar effects, only the peak values method was used, taking into account that the higher sediment transport capacity is associated with waves with higher velocities. In addition, most bed sediment transport formulae were dependent on the squared velocity values. The velocity variability was measured for each BR60 and R60 layout, considering two different comparative analyses: (i) by comparing different time series in a unique layout at the same position and (ii) by comparing them with/without a meadow in the same sensor position and the same test number.

3. Results

3.1. Velocity Variability Induced by Surrogate Seagrass Effect

The values obtained in Table 3 showed the variability of peak velocities. The standard deviations found at positions closer to the bar were higher than those found at positions prior to X = 50.1 m presented in Table 2. At X = 54.2 m the variability values were equal or even higher than for X = 50.1 m, except for the variability of negative peak R60 at tests t7–t9. The larger variabilities observed could be explained by the proximity of the ADV measurements with respect to the breaker bar. The bar was growing between positions X = 59.0 m and X = 57.4 m for R60 (between t6 and t9), and for X = 61.7 m (t6) and X = 61.0 m (t9) for BR60, which would affect the velocity measurements at the nearby control points. The difference between positive and negative peak variability was lower than 0.01 ms^{-1}, except for t7 and t9 comparison for R60 (0.028 ms^{-1}). This narrow difference between positive and negative peak variability followed a similar trend to that observed in Table 2. Table 2 displayed the computed peak variability for the initial profiles (t2, t3, and t4) when the bar had not undergone significant changes. On the other hand, Table 3 includes the computed data for profiles t2 as well as t6-t9, where the bar noticeably moved offshore towards the measurement position (X = 50.2 and 54.2 m). This displacement of the bar, coupled with the closer proximity of the sensors to the bottom of the profile, leads to increased variabilities in peak values when compared to those observed in Table 2.

Table 3. Illustration of the velocity peak variability at a fixed cross-shore position, comparing different tests for each experimental layout.

Position (m)	Case	Test Comparison	Peak (+) Variability (ms^{-1})	Peak (−) Variability (ms^{-1})
X = 50.2	BR60	t6–t8	0.024	0.026
X = 54.2		t2–t7	0.043	0.051
X = 54.2		t2–t9	0.060	0.061
X = 54.2		t7–t9	0.051	0.050
X = 50.2	R60	t6–t8	0.045	0.053
X = 54.2		t2–t7	0.049	0.057
X = 54.2		t2–t9	0.040	0.053
X = 54.2		t7–t9	0.050	0.022

Table 4 compares the u peak variability between the difference of BR60 and R60 layouts at the same time and at three different cross-shore positions. All tests present an equal or lower u peak variability in front of the meadow, while this value is larger behind the meadow. The areas closer to the bar, as presented in Table 3, had a similar variability to the area behind the meadow. At t2, the bar crest is located at X = 59.12 m and X = 60.9 m (BR60 and R60 respectively), so we can see the effects of the surrogate meadows on u, without the perturbations generated by a bar closer to the control point (i.e., X = 54.2 m). Therefore, it can be considered that the changes in u at this time are mainly due to the effect of the

meadow. As the position of the bar moves towards offshore positions, the variability of u increases, and an important part of this variability could be due to the development of the bar. This was observed in X = 54.2 m. In t2, the average of positive and negative variabilities was lower than for t7 and t9. This was also the case at X = 45.7 m and X = 50.2 m, where the average of the variabilities was lower in the initial tests compared to later times. From t6 onwards, there was an increase in the magnitude of the variability of u (negative or positive) in the areas furthest away from the bar, but in each test, the lowest variability was maintained in the area in front of the meadow as opposed to post-meadow areas. In contrast to Tables 1 and 2, the negative and positive peaks showed different variabilities at X = 50.2 m and X = 54.2 m. In these positions, the positive peaks tended to have greater variability than the negative peaks, except for t7. These increases in variability indicate that the studied waves experience relevant changes in their maximum and minimum values.

Table 4. Illustration of velocity peak variability from the variation of BR60 and R60 layouts for different tests and positions.

Position (m)	Test	Peak (+) Variability (ms^{-1})	Peak (−) Variability (ms^{-1})
X = 27.6	t2	0.010	0.010
X = 41.4	t2	0.035	0.014
X = 54.2	t2	0.040	0.016
X = 27.6	t3	0.015	0.017
X = 41.4	t3	0.044	0.010
X = 45.7	t3	0.033	0.027
X = 27.6	t6	0.014	0.019
X = 41.4	t6	0.040	0.023
X = 50.2	t6	0.042	0.026
X = 27.6	t7	0.027	0.035
X = 41.4	t7	0.032	0.038
X = 54.2	t7	0.035	0.041
X = 27.6	t8	0.027	0.033
X = 41.4	t8	0.031	0.023
X = 50.2	t8	0.049	0.032
X = 27.6	t9	0.018	0.021
X = 41.4	t9	0.027	0.020
X = 54.2	t9	0.044	0.028
X = 27.6	t10	0.031	0.022
X = 41.4	t10	0.031	0.031
X = 45.7	t10	0.038	0.044

3.2. Velocity Peak Magnitude

The mean peak (positive and negative) velocities were calculated for BR60 and R60 and are presented in Table 5. The number of peaks studied to obtain the average value are shown in Column 3 of Table 5. Note that the number of peaks compared was between 224 and 375, which corresponds to 73.0% and 95.4% of the total number of waves for both layouts. Positive peaks showed a significant increase in R60 compared to BR60. This increase was between 5.5% and 12.4% in the area in front of the meadow and between 6.5% and 11.7% in the area immediately behind the meadow. In the post-meadow areas (sand slope zone), the effect was the opposite and the velocity decreased to 10.2%, except at t7, where the velocity increased by up to 8.8%. The negative peaks studied showed a different behavior in the meadow area. In the area in front of the meadow, a small positive increase in velocities was observed, ranging from 0.9% to 2.4%. In the area immediately behind the meadow, the positive peaks showed a significant decrease of between 14.0% and 20.3%. Then, in the slope zone, the velocity became more positive, with negative peaks decreasing by as much as 9.1%, except at t6 and t7, where the velocity increased slightly on the R60 line.

Table 5. Velocity peak (positive and negative) values for the BR60 and R60 layouts, showing the variability for different tests and positions.

Position (m)	Series Variability (ms^{-1})	Number of Peaks	Mean Positive Peaks BR60 (ms^{-1})	Mean Positive Peaks R60 (ms^{-1})	Positive Peaks Variation	Mean Negative Peaks BR60 (ms^{-1})	Mean Negative Peaks R60 (ms^{-1})	Negative Peak Variation
X = 27.6	t2	278	0.2932	0.3100	5.7%	0.3055	0.2983	−2.4%
X = 41.4	t2	248	0.3415	0.3718	8.9%	0.3390	0.2717	−19.9%
X = 54.2	t2	370	0.5574	0.5003	−10.2%	0.4693	0.4265	−9.1%
X = 27.6	t3	330	0.2875	0.3032	5.5%	0.3066	0.3017	−1.6%
X = 41.4	t3	333	0.3475	0.3716	7.0%	0.3276	0.2610	−20.3%
X = 45.7	t3	365	0.3627	0.3427	−5.5%	0.3365	0.3200	−4.9%
X = 27.6	t6	333	0.2933	0.3094	5.5%	0.3054	0.2992	−2.0%
X = 41.4	t6	329	0.3441	0.3666	6.5%	0.3330	0.2748	−17.5%
X = 50.2	t6	375	0.4376	0.4336	−0.9%	0.3758	0.3781	0.6%
X = 27.6	t7	259	0.2766	0.3088	11.6%	0.2954	0.2921	−1.1%
X = 41.4	t7	224	0.3495	0.3796	8.6%	0.3444	0.2834	−17.7%
X = 54.2	t7	260	0.5432	0.5908	8.8%	0.4813	0.4923	2.3%
X = 27.6	t8	310	0.2784	0.3130	12.4%	0.3016	0.2988	−0.9%
X = 41.4	t8	310	0.3388	0.3672	8.4%	0.3381	0.2872	−15.1%
X = 50.2	t8	359	0.4532	0.4143	−8.6%	0.3981	0.3669	−7.9%
X = 27.6	t9	317	0.2892	0.3195	10.5%	0.2977	0.3020	1.4%
X = 41.4	t9	324	0.3344	0.3565	6.6%	0.3348	0.2878	−14.0%
X = 54.2	t9	357	0.5693	0.5334	−6.3%	0.5232	0.4580	−12.5%
X = 27.6	t10	268	0.3047	0.3229	6.0%	0.3112	0.3076	−1.2%
X = 41.4	t10	240	0.3459	0.3864	11.7%	0.3361	0.2840	−15.5%
X = 45.7	t10	289	0.3734	0.3407	−8.8%	0.3420	0.3190	−6.7%

Table 5 also showed how the behavior in the meadow areas (in front of/behind the meadow) was similar for both peaks between the t2 and t6 tests. Positive peaks in front of the meadow increased on average by 5.6%, and negative peaks decreased on average by 2.0%. Behind the meadow, positive peaks increased on average by 7.5% and negative peaks decreased on average by 19.2%. Then, for tests t7 to t10 in the area in front of the meadow, the positive values increased on average by 10.1% and the negative values decreased on average by 0.5%. Behind the meadow, positive peaks increased on average by 8.8% while negative peaks decreased on average by 15.5%.

3.3. Asymmetry and Skewness Changes along the Flume Caused by Surrogate Seagrass Effect

The values obtained for *Sk* and *As* in positions in front of, above, and behind the meadow, at the same height relative to the bottom (Z_R), are shown in Figures 4 and 5. Figure 4 illustrates that in BR60 and R60, *Sk* values did not exhibit relevant variability at X = 27.6 m and X = 31.9 m. Beyond these initial positions, at X = 39.1 m and X = 41.4 m, *Sk* became slightly more positive when the meadow was present. Additionally, the *As* values in front of and behind the meadow were very similar for each compared layout. Above the meadow area, there was a small increase in *As* when the meadow was present, although this value was too low (less than 0.005) to be considered relevant.

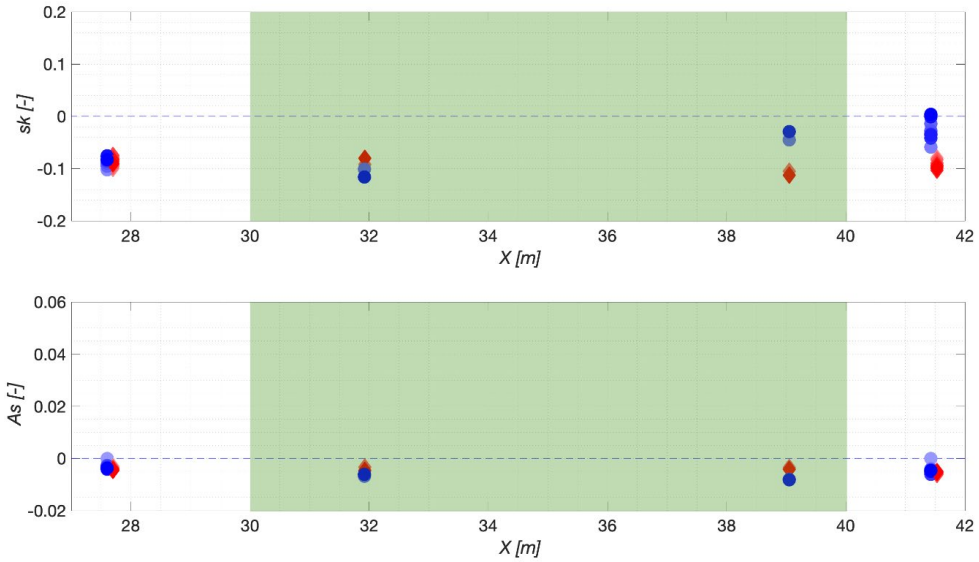

Figure 4. Illustration of skewness (*Sk*) and asymmetry (*As*) variation (bottom and top panel respectively) for measuring stations between X = 27.6 m and X = 41.4 m. Red diamonds represent the BR60 layout and blue circles represent the R60 layout. The lighter shades represent the initial tests, and the darker shades represent the final tests, as detailed in Figure 2. X = 31.9 m corresponds to measurements at t5 and t12, while X = 39.1 m corresponds to measurements at t4 and t11. The green area represents the meadow zone located between X = 30 m and X = 40 m.

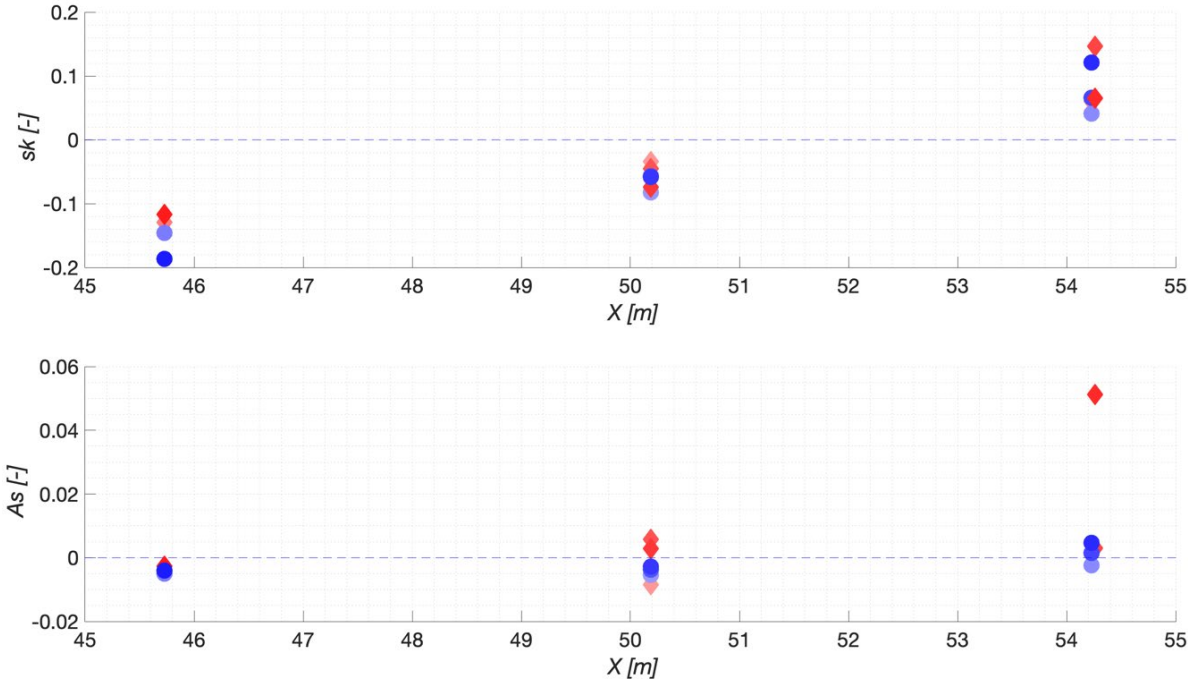

Figure 5. Illustration of skewness (*Sk*) and asymmetry (*As*) variation (bottom and top panel respectively) for measuring stations between X = 45.7 m and X = 54.2 m. Red diamonds represent the BR60 layout, and blue circles represent the R60 layout. The lighter shades represent the initial tests, and the darker shades represent the final tests, as detailed in Figure 2. X = 45.7 m corresponds to measurements at t3 and t10, while X = 50.1 m corresponds to measurements at t6 and t8, and X = 54.2 m corresponds to t2, t7, t9.

Along the slope that follows the meadow (Figure 5), there is a *Sk* decrease at X = 45.7 m for the R60 layout for t3 and t10, higher than the decrease measured for the same tests for the BR60 layout. Once the velocity values were considered closer to the bar, the *Sk* value became more positive for both BR60 and R60 layouts, with the *Sk* values being greater than 0 at X = 54.2 m.

The *As* value at X = 45.7 m was still similar in value to X = 27.6 m and X = 41.4 m, with slightly negative values for this layout. At X = 50.2 m for the R60 layout, the value of *As* was constant and similar to the previous position, but for the BR60 layout at t6 and t8, the value became slightly positive. The *As* value at X = 54.2 m for t7 remained slightly positive for both layouts. At t9, this *As* value was maintained for R60, but increased to 0.05 at BR60 (red diamonds in Figure 5 below).

3.4. Sediment Transport Capacity

Considering the observed changes in wave shape and velocity due to the presence of the mimic seagrass meadow, the sediment transport capacity was evaluated following the SANTOSS formula [62] detailed in Equation (6).

$$\vec{q}_s = \sqrt{(s-1) \times g \times d_{50}^3} \times \frac{\sqrt{|\theta_c|} \times T_c \times \left(\Omega_{cc} + \frac{T_c}{2 \times T_{cu}} \times \Omega_{tc}\right) \times \frac{\vec{\theta}_c}{|\theta_c|} + \sqrt{|\theta_t|} \times T_t \times \left(\Omega_{tt} + \frac{T_t}{2 \times T_{tu}} \times \Omega_{tu}\right) \times \frac{\vec{\theta}_t}{|\theta_t|}}{T} \quad (6)$$

where $\vec{q}_s$ is the capacity net transport rate ($m^2\ s^{-1}$), s is the relative density equal to $(\delta_S - \delta_W)/\delta_W$, d_{50} is the median grain size (m), g is the gravitational acceleration (ms^{-2}), θ is the non-dimensional bed shear stress (Shield Parameter) and T the wave period (s), with "c" referring to the crest and "t" to the trough of the half-wave cycle. T_{cu} and T_{tu} are the acceleration flow periods within the crest/trough half cycle, respectively. The variables Ω_{cc}, Ω_{tc}, Ω_{tt}, and Ω_{ct} represent a contribution to the net transport rates, where the first sub-index denotes the sand load mobilized for the half cycle (crest/trough) and the second sub-index represents the sand transported during the half cycle (crest/trough). These four contributions to net sand transport depend on the Shields parameter, and the methodology of [62] has been followed to calculate them.

The q_s values were calculated taking into account the mean velocities, the average of the highest one-third velocities (1/3), and the average of the highest one-tenth velocities (1/10) at each position shown in Figure 6 (X = 27.6, 41.2, 45.7, 50.2 and 54.2 m). The calculated net transport was onshore at all positions and increased gradually as one moved towards the coast and according to the magnitudes of the velocities studied. The sediment transport capacity was lower for the meadow layout (R60, blue diamonds in Figure 7), except for the first measurement position found in front of the meadow. The percentage decrease in sediment transport capacity obtained for each position is shown in Table 6. Although a significant reduction in sediment transport capacity was observed at the positions from X = 27.6 m to X = 50.2 m (grey values in Table 6), it is important to note that transport in this area experiences substantially lower magnitudes if we compare it with positions beyond X = 54 m.

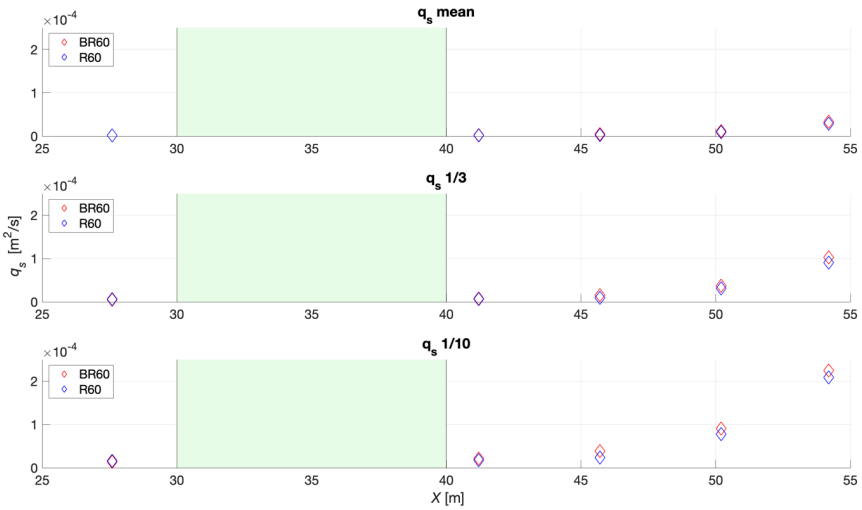

Figure 6. Representative q_s values at each measurement station considered for mean, 1/3 and 1/10 velocities. The blue diamond represents the R60 layout, and the red diamond represents the BR60 layout. The green area indicates the seabed meadow zone.

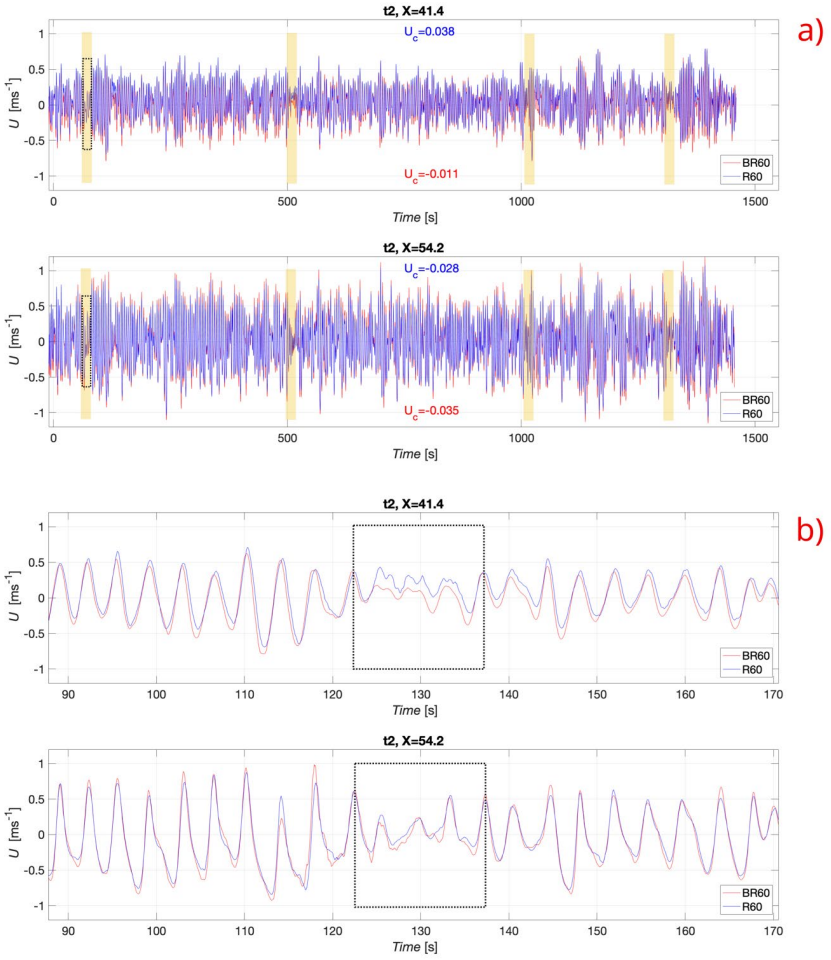

Figure 7. (**a**) Time series of u in Test 2 for positions X = 41.4 m (upper panel) and X = 54.2 m (lower panel), indicating with a yellow rectangle the major divergences found in the whole series. The BR60 layout is shown in red and the R60 layout in blue. The U_c values for the whole t2 series are presented in the figure, keeping the colors of each layout for consistency. (**b**) Details of a case of velocity divergence (black dashed lines in Figure 7a,b) between 125 and 135 s.

Table 6. Variation of q_s (%) when comparing R60 with BR60 layouts in the same cross-profile positions for different velocities.

	X = 27.6 m	X = 41.2 m	X = 45.7 m	X = 50.2 m	X = 54.2 m
Mean	18.3%	−18.9%	−41.3%	−15.3%	−13.2%
1/3	29.3%	−11.6%	−40.8%	−15.0%	−11.9%
1/10	18.9%	−17.1%	−39.0%	−14.0%	−7.1%

4. Discussion

The presence of a surrogate seagrass meadow in a series of mobile bed flume experiments leads to an increase in the current velocity (U_c) measured in the area immediately in front of and behind the meadow. In front of the meadow, U_c increases slightly by 0.012 ms^{-1} (78.7%) on average over the experimental time (6 h of waves). Behind the meadow zone, U_c increases significantly by 0.049 ms^{-1} (365.4%) on average. Although the observed increase in values in front of the meadow are within the range of the sensor variability (Table 2), the increase in U_c behind the meadow is above this variability and can be attributed to a direct effect of the seagrass meadow studied. These results are consistent with previous studies that assessed velocities around the seagrass canopy in areas upstream [63] and downstream of the meadow [45,49,63,64]. This U_c could be explained by the velocity overshoot produced by a progressive wave above the boundary layer and by the progressive wave streaming expected within the boundary layer. Although the measurement point is not within the boundary layer, the presence of the oscillating bending long leaves and their associated turbulence is expected to increase the thickness of the wave boundary layer and therefore increase the shoreward velocity streaming produced by both effects. However, this experiment did not provide the necessary data to confirm such behavior.

The sensor variabilities shown in Table 2 are slightly higher than the variabilities measured by the ADV in the comparatively quiescent background (-0.006 ± 0.006 ms^{-1}), calculated in the first 5 s after the start of each test. These values were associated with white noise or Doppler noise and are intrinsic to the ADV [65]. However, the measured changes in peak velocities (Table 5) are greater than the sensor variabilities (Table 2). The variations of both maximum and minimum velocities are attributed to the presence of the meadow and the development of the breaker bar. The latter can be seen more clearly from t7 (3.5 h of waves), where the peak variabilities in front of the meadow increase their value (Table 4) and the positive peaks increase their velocities even more with respect to previous times (Table 5). The variability in velocity intensity and peaks can be observed in all tests and could be associated with the direct effect of the meadow.

In the area in front of the meadow, there is no appreciable change in *Sk* and *As* compared to the case without the meadow throughout all tests. The mean value of *As* for 12 tests was −0.004 for BR60 and −0.003 for R60, and the mean value of *Sk* was −0.087 for both layouts. Despite this, up to t6, there was an increase in positive peak velocities (mean 5.6%) and a slight reduction in negative peak velocities (mean 2.0%), without this affecting the magnitude of mean velocities (mean positive peak plus mean negative peak), resulting in changes of less than 0.010 ms^{-1}.

Above the meadow, it is observed that *Sk* values show little variation between layouts at the beginning, while *As* was slightly reduced when the meadow was present. At the end of the meadow, the *Sk* value increased for R60, while *As* decreased. Studies such as that of [49] have also observed a decrease in *As* inside a mimic seagrass meadow patch and have found in their research that the larger the patch size, the greater the *As* decrease. In addition, *Sk* values increase when the surrogate meadow is present, but only under the most energetic waves, with an even greater increase when the patch covered a smaller area [49].

In the area behind the meadow, a shift of the whole u-series towards the positive axis can be observed, which is associated with the increase in U_c. Additionally, there is an increase of 0.1 in *Sk* compared to the BR60 layout, which is associated with a vertical deformation of the incoming waves. This effect is confirmed by the increase of positive

peaks and the reduction of negative peaks under the waves (Table 5), which adjusted to a new waveform when passing through the meadow. This implies that onshore velocities are higher, while offshore velocities are lower in magnitude than in the case without the surrogate meadow. *As* values remain unchanged and behave similarly to the *As* data obtained in front of the meadow.

The discrepancies in *Sk* behind the meadow have been analyzed for the entire velocity series, comparing different layouts within the same test number and sensor position. Figure 7a shows the velocity series measurements at the same location and time (time series t2) for both layouts. The upper and lower parts of Figures 7a and 6b correspond to positions X = 41.4 m and X = 54.2 m, respectively. At X = 41.4 m (Figure 7a), a positive shift of the entire u-series can be observed when comparing layouts BR60 and R60, indicating an increase in the magnitude of positive peak values and a decrease in the magnitude of negative peak values when the meadow is present. Additionally, this increase in u is more pronounced in 4 points associated with wave relaxation periods. The upper part of Figure 7b provides an example of this further increase in u between times 123 and 137 s when the meadow is present, causing a significant rise in the velocities of low-magnitude flows. However, these changes in wave relaxation are not observed at more onshore positions, as illustrated in the lower part of Figure 7b, which presents the velocity measurements at X = 54.2 m.

As the position of the bar crest approaches the ADV control point, the value of *Sk* becomes more positive. At X = 45.7 m, layout R60 exhibits a slightly lower *Sk* compared to BR60, with both layouts showing lower magnitudes than when measured at positions in front of the meadow. The changes in peak velocities at this position experience a similar variation, with reduced maximum and minimum peaks in R60 with respect to BR60. At this location, the wave velocities take on a similar shape as in positions at X = 27.6 m but with a decrease in velocity magnitude in R60 relative to BR60.

At X = 50.2 m, the differences in *Sk* values between both layouts are even smaller than at X = 45.7 m, but their magnitude increases with respect to this position. The minimum and maximum peaks are similarly reduced. At t6, the peak velocities show a variation of less than 1.0% when comparing the two layouts, but at t8 the reduction of positive peaks is 8.6% and negative peaks decrease by 7.9% when the meadow is present. This velocity reduction is consistent with the results from the previous position.

Finally, at X = 54.2 m, a general decrease in the maximum and minimum u magnitudes (lower part of Figure 7b) associated with a reduction in the magnitude of both maximum and minimum peaks can be observed when seagrass is present. Additionally, registered *Sk* values turned positive and are higher at BR60 than at o R60, where both negative and positive peaks are reduced, except at t7 where they increase. This progressive increase in *Sk* values reflects the change in wave shape as it passes through the shoaling to the breaking bar zone. However, *As* values do not show significant variations in the same area, except at position X = 54.2 m where it becomes slightly positive. It is worth noting that at t9 for the BR60 layout, *As* presents a greater increase compared to other times and positions (Figure 5). In this test, the position of the bar crest (X = 56.4 m) is very close to the control point, so the wave starts to accelerate shorewards to generate a breaking wave. In the R60 layout, this process does not occur at this position but takes place two meters further onshore. The greater increase in *As* of BR60 is attributable to a greater increase in sediment transport found where the bar is developing (See Figure 6). This is consistent with previous studies [66–68] that have shown that higher *As* is correlated with a higher rate of sediment transport in the direction of wave propagation.

In summary, the presence of the meadow causes variations in velocities due to the enhanced resistance it offers to wave propagation. This resistance leads to lower *As* values as the waves pass through the meadow, resulting in higher magnitudes of offshore velocities. The *Sk* values increase as the waves pass through the meadow and become positive upon leaving the meadow (Figure 4). This destabilizes the velocity series due to increased currents generated behind the meadow. As a result, there appear losses of

potential energy (reduction of wave height) and kinetic energy (reduction of velocities), the latter of greater magnitude [47]. In subsequent zones, the decreased velocity has stabilized, and variations of *Sk* and *As* are dominated by the displacement of the offshore bar crest (breaking wave area).

The transport capacity calculated by the SANTOSS formula has been compared with the volume of sediment transported at position X = 54.2 m in tests t2, t7, and t9 for each layout (Table 7). The sediment volume has been quantified from the bed evolution of each test, measured with a mechanical profiler, as detailed in [47] Astudillo et al., 2022. The sediment transport obtained by both methods was in the onshore direction. The values obtained by the SANTOSS formula for the BR60 layout were close to those measured in the experiments. However, for the R60 layout, the calculated values exhibited larger discrepancies compared to the measured values. At t2, the measured sediment transport is greater than that estimated by the SANTOSS formula and is attributed to the sensor being located over one of the megaripple-like bedforms generated in the sandy profile. While at t7, it was observed that the presence of seagrass induces a larger amount of transported sediment, which is consistent with the peak velocities found in this test (Table 5), where the R60 layout presents higher values than the BR60 layout. The increased velocity peaks in t7 cannot be conclusively explained within the scope of this work since they may be attributed to measurement errors or to the larger morphodynamic stability for dissipative profiles with bedforms.

Table 7. Critical comparison of q_s measured and calculated values for BR60 and R60 layouts at position X = 54.2 m.

	MEASURED			SANTOSS		
Test	**BR60 (m^2 s^{-1})**	**R60 (m^2 s^{-1})**	**Variation (%)**	**BR60 (m^2 s^{-1})**	**R60 (m^2 s^{-1})**	**Variation (%)**
t2	3.56×10^{-5}	5.72×10^{-5}	60.7	3.59×10^{-5}	1.77×10^{-5}	−50.7
t7	5.52×10^{-5}	1.72×10^{-5}	−68.8	2.07×10^{-5}	4.11×10^{-5}	98.9
t9	4.44×10^{-5}	1.72×10^{-5}	−61.3	4.34×10^{-5}	2.81×10^{-5}	−35.4
Mean (t2–t7–t9)	4.51×10^{-5}	3.05×10^{-5}	−32.2	3.33×10^{-5}	2.90×10^{-5}	−13.2

Note that the sediment transport at t2 is higher at R60 compared to BR60 layout, again this is attributed to megaripple-like bedforms. These megaripple-like bedforms appeared first in R60 (t2), and then in BR60 (t5), and remained in the same position and shape until they were eventually absorbed by the main bar moving offshore (Figure 8). Although the SANTOSS equation considers values from an empirical ripple generator, it should be emphasised that sediment transport in rippled bottoms is notoriously difficult to predict [62]. The SANTOSS formula is unable to reproduce the position where the megaripple-like bedforms are generated, indicating that the sediment transport capacity at this point and test may not have been correctly estimated. However, the formula still provides valuable insight, suggesting that sediment transport in this area, after the formation of the megaripple-like bedforms, is very low.

The profile evolution, including megaripple-like bedforms, could be related to *Sk* changes in the waves, as observed [69] in the case of submerged berms subjected to irregular waves. Therefore, the formation of megaripple-like bedforms at t2 for the R60 layout could be associated with the *Sk* changes induced by the presence of the meadow. Similarly, the development of the bar in the BR60 layout between t4 and t5, which in turn generates higher *Sk* values, could potentially explain the subsequent appearance of these bedforms. However, it should be noted that the available data set is limited, and further investigation is needed to confirm this behavior.

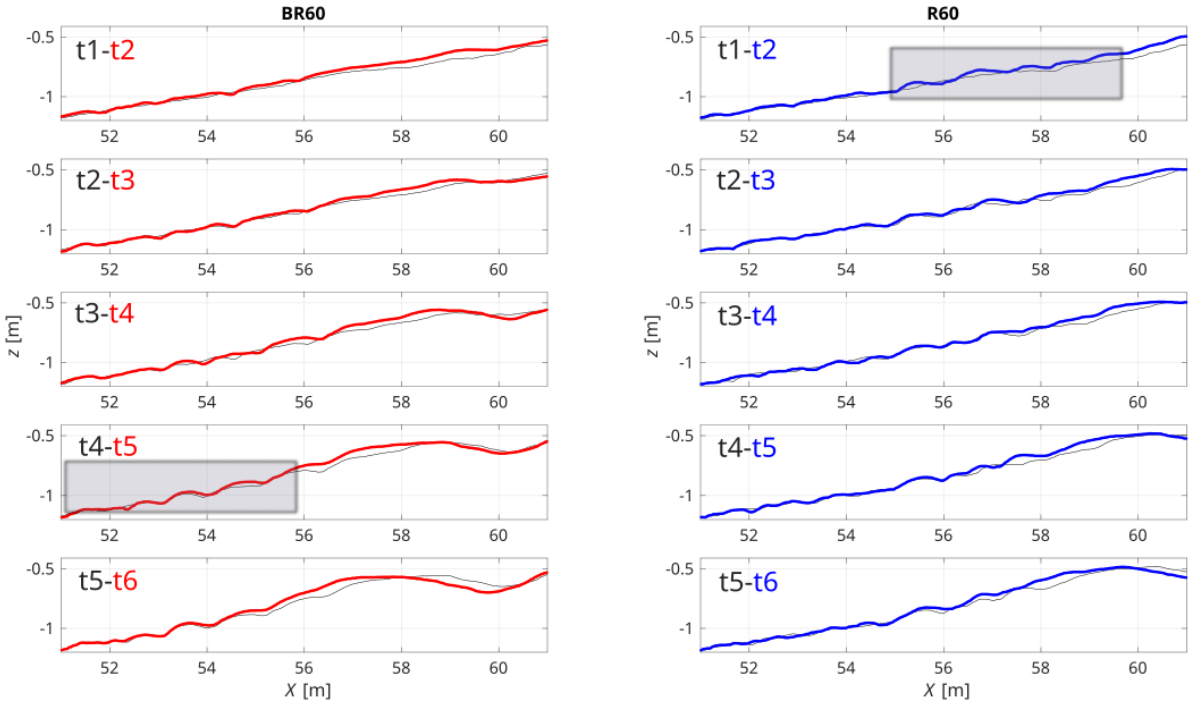

Figure 8. Sand profile evolution for BR60 (**left** panels) and R60 (**right** panels) experimental layouts. Black lines indicate the profile evolution for the initial test comparison, while red and blue lines indicate the profile evolution for the subsequent test comparison for BR60 and R60, respectively. The grey areas indicate the occurrence of megaripple-like bedforms in each layout.

5. Conclusions

The present study contributes to analyze the interactions between incoming waves and seagrass meadows, demonstrating the effect of the meadow on the velocities generated by irregular erosive waves. The analysis compares the velocity fields over a seagrass meadow, considering the hydrodynamic behavior up to the main sandbar. The results presented lead to the following conclusions:

The passage of the waves over the meadow causes a large decrease/increase in the magnitude of negative/positive velocity peaks. This interaction effect results in two important changes for the velocities: (i) a change in the way velocities propagate, generating higher velocities onshore and even lower velocities offshore; (ii) in the first few meters of the sandy slope, where the velocities returned to their original shape in front of the meadow but with a decrease in their overall magnitude. The observed interaction thus makes the incoming erosive waves less erosive with less sediment transport, resulting in a bar closer to the shoreline.

As the waves passed through the surrogate seagrass meadow, there is a gradual increase in *Sk*, with a local maximum value in the area behind the meadow. However, as the wave evolves along the sandy slope, the *Sk* value decreases, reaching a minimum value even lower than before the presence of the meadow. Finally, as the control position approaches the breaker bar, the *Sk* value gradually increases. In conditions without a meadow, the *Sk* values remain stable until the measurement station X = 50.2 m, where the *Sk* value increases because of its proximity to the position of the main bar.

The influence of the meadow on the *As* variation is found to be small, with only a slight reduction observed in the area above the meadow. However, a significant increase in *As* is observed when the control (measurement) point gets closer to the position of the bar. This increase is primarily attributed to the proximity of the waves' breaking position and is not directly influenced by the surrogate meadow.

The decrease in velocities induced by the meadow diminishes the offshore sediment transport in the sand part of the profile. While the SANTOSS formula was able to provide a suitable estimate of sediment transport, it could not approximate the sediment volumes of the bedforms generated in the profile. Additionally, the changes in *Sk* caused by the presence of the meadow result in the earlier appearance of megaripple-like bedforms in the profile area in front of the main bar.

Author Contributions: Conceptualization, C.A.-G., I.C.R., V.G.G., J.P.S.P. and A.S.-A.C.; Methodology, C.A.-G., I.C.R., V.G.G., J.P.S.P. and A.S.-A.C.; Software, C.A.-G. and I.C.R.; Validation, C.A.-G. and I.C.R.; Formal analysis, C.A.-G.; Investigation, C.A.-G.; Data curation, C.A.-G. and I.C.R.; Writing—original draft, C.A.-G.; Writing—review & editing, C.A.-G., I.C.R. and A.S.-A.C.; Visualization, C.A.-G.; Supervision, I.C.R., V.G.G. and J.P.S.P.; Project administration, V.G.G. and J.P.S.P.; Funding acquisition, V.G.G., J.P.S.P. and A.S.-A.C. All authors have read and agreed to the published version of the manuscript.

Funding: The laboratory experiments described in this research were funded by the Spanish Government within the Research, Development and Innovation Program through a grant to the ECOPLANTS project (REF PID2020-119058RB-I00). The REST-COAST project receives funding from the European Union's Horizon 2020 Research and Innovation action under grant agreement No 101037097. The first author acknowledges funding from the National Agency for Research and Development (ANID)/Scholarship Program/DOCTORADO BECAS CHILE/2018-72190552.

Institutional Review Board Statement: Not applicable.

Informed Consent Statement: Not applicable.

Data Availability Statement: Data available upon request to the authors.

Acknowledgments: This work acknowledges the REST-COAST project, which provided relevant information on the seagrass meadows located off the Catalan coast. We wish to thank the technical staff of the CIEM wave flume (UPC) for their support and contributions to the experiments: Joaquim Sospedra, Oscar Galego, and Ricardo Torres. We would like to express our gratitude to PLÀNCTON, DIVULGACIÓ I SERVEIS MARINS SCP for providing us with an unpublished photograph of a Posidonia oceanica meadow in the Mediterranean sea (Figure 1a).

Conflicts of Interest: The authors declare no conflict of interest.

References

1. Neumann, B.; Vafeidis, A.T.; Zimmermann, J.; Nicholls, R.J. Future coastal population growth and exposure to sea-level rise and coastal flooding-a global assessment. *PLoS ONE* **2015**, *10*, e0118571. [CrossRef] [PubMed]
2. Nicholls, R.J.; Woodroffe, C.; Burkett, V. Coastline Degradation as an Indicator of Global Change. In *Climate Change: Observed Impacts on Planet Earth*, 2nd ed.; Letcher, T.M., Ed.; Elsevier: Amsterdam, The Netherlands, 2016; pp. 309–324. [CrossRef]
3. Nicholls, R.; Townend, I.; Bradbury, A.; Ramsbottom, D.; Day, S. Planning for long-term coastal change: Experiences from England and Wales. *Ocean Eng.* **2013**, *71*, 3–16. [CrossRef]
4. Toimil, A.; Losada, I.J.; Nicholls, R.J.; Dalrymple, R.A.; Stive, M.J. Addressing the challenges of climate change risks and adaptation in coastal areas: A review. *Coast. Eng.* **2020**, *156*, 103611. [CrossRef]
5. Arnoux, F.; Abadie, S.; Bertin, X.; Kojadinovic, I. Coastal flooding event definition based on damages: Case study of Biarritz Grande Plage on the French Basque coast. *Coast. Eng.* **2021**, *166*, 103873. [CrossRef]
6. Ruggiero, P. Is the Intensifying Wave Climate of the U.S. Pacific Northwest Increasing Flooding and Erosion Risk Faster Than Sea-Level Rise? *J. Waterw. Port, Coastal, Ocean Eng.* **2013**, *139*, 88–97. [CrossRef]
7. Sanò, M.; Jiménez, J.; Medina, R.; Stanica, A.; Sanchez-Arcilla, A.; Trumbic, I. The role of coastal setbacks in the context of coastal erosion and climate change. *Ocean Coast. Manag.* **2011**, *54*, 943–950. [CrossRef]
8. Villatoro, M.; Silva, R.; Méndez, F.; Zanuttigh, B.; Pan, S.; Trifonova, E.; Losada, I.; Izaguirre, C.; Simmonds, D.; Reeve, D.; et al. An approach to assess flooding and erosion risk for open beaches in a changing climate. *Coast. Eng.* **2014**, *87*, 50–76. [CrossRef]
9. Xie, D.; Zou, Q.-P.; Mignone, A.; MacRae, J.D. Coastal flooding from wave overtopping and sea level rise adaptation in the northeastern USA. *Coast. Eng.* **2019**, *150*, 39–58. [CrossRef]
10. Dong, W.S.; Ariffin, E.H.; Saengsupavanich, C.; Rashid, M.A.M.; Shukri, M.H.M.; Ramli, M.Z.; Miskon, M.F.; Jeofry, M.H.; Yunus, K.; Ghazali, N.H.M.; et al. Adaptation of Coastal Defence Structure as a Mechanism to Alleviate Coastal Erosion in Monsoon Dominated Coast of Peninsular Malaysia. *J. Environ. Manag.* **2023**, *333*, 117391.
11. Fankhauser, S. Protection versus retreat: The economic costs of sea-level rise. *Environ. Plan. A* **1995**, *27*, 299–319. [CrossRef]

12. Rashidi, A.H.M.; Jamal, M.H.; Hassan, M.Z.; Sendek, S.S.M.; Sopie, S.L.M.; Hamid, M.R.A. Coastal structures as beach erosion control and sea level rise adaptation in Malaysia: A review. *Water* **2021**, *13*, 1741. [CrossRef]
13. Schoonees, T.; Mancheño, A.G.; Scheres, B.; Bouma, T.J.; Silva, R.; Schlurmann, T.; Schüttrumpf, H. Hard Structures for Coastal Protection, Towards Greener Designs. *Estuaries Coasts* **2019**, *42*, 1709–1729. [CrossRef]
14. Yohe, G.; Tol, R.S. Indicators for social and economic coping capacity—Moving toward a working definition of adaptive capacity. *Glob. Environ. Chang.* **2002**, *12*, 25–40. [CrossRef]
15. Sales, R.F.M. Vulnerability and adaptation of coastal communities to climate variability and sea-level rise: Their implications for integrated coastal management in Cavite City, Philippines. *Ocean Coast. Manag.* **2009**, *52*, 395–404. [CrossRef]
16. Stancheva, M.; Rangel-Buitrago, N.; Anfuso, G.; Palazov, A.; Stanchev, H.; Correa, I. Expanding Level of Coastal Armouring: Case Studies from Different Countries. *J. Coast. Res.* 2011, pp. 1815–1819. Available online: http://www.jstor.org/stable/26482490 (accessed on 15 March 2023).
17. Foti, E.; Musumeci, R.E.; Stagnitti, M. Coastal defence techniques and climate change: A review. *Rend. Lince- Sci. Fis. e Nat.* **2020**, *31*, 123–138. [CrossRef]
18. Hanak, E.; Moreno, G. California coastal management with a changing climate. *Clim. Chang.* **2012**, *111*, 45–73. [CrossRef]
19. Jonkman, S.N.; Hillen, M.M.; Nicholls, R.J.; Kanning, W.; van Ledden, M. Costs of adapting coastal defences to Sea-Level Rise—New Estimates and Their Implications. *J. Coast. Res.* **2013**, *29*, 1212–1226. [CrossRef]
20. Morris, R.; Strain, E.M.A.; Konlechner, T.M.; Fest, B.J.; Kennedy, D.M.; Arndt, S.K.; Swearer, S.E. Developing a nature-based coastal defence strategy for Australia. *Aust. J. Civ. Eng.* **2019**, *17*, 167–176. [CrossRef]
21. Borsje, B.W.; van Wesenbeeck, B.K.; Dekker, F.; Paalvast, P.; Bouma, T.J.; van Katwijk, M.M.; de Vries, M.B. How ecological engineering can serve in coastal protection. *Ecol. Eng.* **2011**, *37*, 113–122. [CrossRef]
22. Spalding, M.D.; Ruffo, S.; Lacambra, C.; Meliane, I.; Hale, L.Z.; Shepard, C.C.; Beck, M.W. The role of ecosystems in coastal protection: Adapting to climate change and coastal hazards. *Ocean Coast. Manag.* **2014**, *90*, 50–57. [CrossRef]
23. Strain, E.; Kompas, T.; Boxshall, A.; Kelvin, J.; Swearer, S.; Morris, R. Assessing the coastal protection services of natural mangrove forests and artificial rock revetments. *Ecosyst. Serv.* **2022**, *55*, 101429. [CrossRef]
24. Temmerman, S.; Govers, G.; Wartel, S.; Meire, P. Modelling estuarine variations in tidal marsh sedimentation: Response to changing sea level and suspended sediment concentrations. *Mar. Geol.* **2004**, *212*, 1–19. [CrossRef]
25. Webb, A.P.; Kench, P.S. The dynamic response of reef islands to sea-level rise: Evidence from multi-decadal analysis of island change in the Central Pacific. *Glob. Planet. Chang.* **2010**, *72*, 234–246. [CrossRef]
26. Chastel, T.; Botten, K.; Durand, N.; Goutal, N. Bulk drag coefficient of a subaquatic vegetation subjected to irregular waves: Influence of Reynolds and Keulegan-Carpenter numbers. *La Houille Blanche* **2020**, *106*, 34–42. [CrossRef]
27. Manca, E.; Cáceres, I.; Alsina, J.; Stratigaki, V.; Townend, I.; Amos, C. Wave energy and wave-induced flow reduction by full-scale model Posidonia oceanica seagrass. *Cont. Shelf Res.* **2012**, *50-51*, 100–116. [CrossRef]
28. Maza, M.; Lara, J.L.; Losada, I.J. Advances in Water Resources Experimental analysis of wave attenuation and drag forces in a realistic fringe Rhizophora mangrove forest. *Adv. Water Resour.* **2019**, *131*, 103376. [CrossRef]
29. Astudillo-Gutierrez, C.; Gracia, V.; Cáceres, I.; Sierra, J.P.; Sánchez-Arcilla, A. Influence of seagrass meadow length on beach morphodynamics: An experimental study. *Sci. Total. Environ.* **2024**, *921*, 170888. [CrossRef] [PubMed]
30. Marinho, B.; Coelho, C.; Hanson, H.; Tussupova, K. Coastal management in Portugal: Practices for reflection and learning. *Ocean Coast. Manag.* **2019**, *181*, 104874. [CrossRef]
31. Saengsupavanich, C.; Chonwattana, S.; Naimsampao, T. Coastal erosion through integrated management: A case of Southern Thailand. *Ocean Coast. Manag.* **2009**, *52*, 307–316. [CrossRef]
32. Singhvi, A.; Luijendijk, A.P.; van Oudenhoven, A.P. The grey–green spectrum: A review of coastal protection interventions. *J. Environ. Manag.* **2022**, *311*, 114824. [CrossRef]
33. Twomey, A.J.; Callaghan, D.P.; O'Brien, K.R.; Saunders, M.I. Contextualising shoreline protection by seagrass using lessons from submerged breakwaters. *Estuar. Coast. Shelf Sci.* **2022**, *276*, 108011. [CrossRef]
34. Costanza, R.; De Groot, R.; Sutton, P.; Van Der Ploeg, S.; Anderson, S.J.; Kubiszewski, I.; Farber, S.; Turner, R.K. Changes in the global value of ecosystem services. *Glob. Environ. Chang.* **2014**, *26*, 152–158. [CrossRef]
35. De Groot, R.; Brander, L.; Van Der Ploeg, S.; Costanza, R.; Bernard, F.; Braat, L.; Christie, M.; Crossman, N.; Ghermandi, A.; Hein, L.; et al. Global estimates of the value of ecosystems and their services in monetary units. *Ecosyst. Serv.* **2012**, *1*, 50–61. [CrossRef]
36. Liu, D.; Xu, Y.; Faghihinia, M.; Kay, P.; Chan, F.K.S.; Wu, N. Evolving framework of studies on global gulf ecosystems with Sustainable Development Goals. *Environ. Sci. Pollut. Res.* **2022**, *29*, 18385–18397. [CrossRef] [PubMed]
37. Narayan, S.; Beck, M.W.; Reguero, B.G.; Losada, I.J.; van Wesenbeeck, B.; Pontee, N.; Sanchirico, J.N.; Ingram, J.C.; Lange, G.-M.; Burks-Copes, K.A. The Effectiveness, Costs and Coastal Protection Benefits of Natural and Nature-Based Defences. *PLoS ONE* **2016**, *11*, e0154735. [CrossRef] [PubMed]
38. Ondiviela, B.; Losada, I.J.; Lara, J.L.; Maza, M.; Galván, C.; Bouma, T.J.; van Belzen, J. The role of seagrasses in coastal protection in a changing climate. *Coast. Eng.* **2014**, *87*, 158–168. [CrossRef]
39. Sanchez-Vidal, A.; Canals, M.; de Haan, W.P.; Romero, J.; Veny, M. Seagrasses provide a novel ecosystem service by trapping marine plastics. *Sci. Rep.* **2021**, *11*, 254. [CrossRef]
40. Fonseca, M.; Fisher, J.; Zieman, J.; Thayer, G. Influence of the seagrass, Zostera marina L., on current flow. *Estuar. Coast. Shelf Sci.* **1982**, *15*, 351–364. [CrossRef]

41. Koch, E.W.; Barbier, E.B.; Silliman, B.R.; Reed, D.J.; Perillo, G.M.; Hacker, S.D.; Granek, E.F.; Primavera, J.H.; Muthiga, N.; Polasky, S.; et al. Non-linearity in ecosystem services: Temporal and spatial variability in coastal protection. *Front. Ecol. Environ.* **2009**, *7*, 29–37. [CrossRef]
42. Christianen, M.J.A.; van Belzen, J.; Herman, P.M.J.; van Katwijk, M.M.; Lamers, L.P.M.; van Leent, P.J.M.; Bouma, T.J. Low-Canopy Seagrass Beds Still Provide Important Coastal Protection Services. *PLoS ONE* **2013**, *8*, e62413. [CrossRef]
43. Gacia, E.; Duarte, C. Sediment retention by a mediterranean posidonia oceanica meadow: The balance between deposition and resuspension. *Estuar. Coast. Shelf Sci.* **2001**, *52*, 505–514. [CrossRef]
44. Infantes, E.; Orfila, A.; Simarro, G.; Terrados, J.; Luhar, M.; Nepf, H. Effect of a seagrass (Posidonia oceanica) meadow on wave propagation. *Mar. Ecol. Prog. Ser.* **2012**, *456*, 63–72. [CrossRef]
45. Hu, Z.; Suzuki, T.; Zitman, T.; Uittewaal, W.; Stive, M. Laboratory study on wave dissipation by vegetation in combined current–wave flow. *Coast. Eng.* **2014**, *88*, 131–142. [CrossRef]
46. Prinos, P.; Stratigaki, V.; Manca, E.; Losada, I.; López Lara, J.; Sclavo, M.; Cáceres Rabionet, I.; Sánchez-Arcilla Conejo, A. Wave propagation over posidonia oceanica: Large scale experiments. In Proceedings of the 7th HYDRALAB III Joint Transnational Access User Meeting, Hanover, Germany, 2–4 February 2010; pp. 57–60.
47. Astudillo, C.; Gracia, V.; Cáceres, I.; Sierra, J.P.; Sánchez-Arcilla, A. Beach profile changes induced by surrogate Posidonia Oceanica: Laboratory experiments. *Coast. Eng.* **2022**, *175*, 104144. [CrossRef]
48. Schaefer, R.B.; Nepf, H. Wave damping by seagrass meadows in combined wave-current conditions. *Limnol. Oceanogr.* **2022**, *67*, 1554–1565. [CrossRef]
49. Holzenthal, E.R.; Wengrove, M.E.; Hill, D.F. Mechanisms of sediment transport around finite patches of submerged aquatic vegetation. *Estuar. Coast. Shelf Sci.* **2022**, *273*, 107905. [CrossRef]
50. Pujol, D.; Serra, T.; Colomer, J.; Casamitjana, X. Flow structure in canopy models dominated by progressive waves. *J. Hydrol.* **2013**, *486*, 281–292. [CrossRef]
51. Stratigaki, V.; Manca, E.; Prinos, P.; Losada, I.J.; Lara, J.L.; Sclavo, M.; Amos, C.L.; Cáceres, I.; Sánchez-Arcilla, A. Large-scale experiments on wave propagation over *Posidonia oceanica*. *J. Hydraul. Res.* **2011**, *49*, 31–43. [CrossRef]
52. Thomas, R.E.; Johnson, M.F.; Frostick, L.E.; Parsons, D.R.; Bouma, T.J.; Dijkstra, J.T.; Eiff, O.; Gobert, S.; Henry, P.-Y.; Kemp, P.; et al. Physical modelling of water, fauna and flora: Knowledge gaps, avenues for future research and infrastructural needs. *J. Hydraul. Res.* **2014**, *52*, 311–325. [CrossRef]
53. Folk, R.L. A review of grain-size parameters. *Sedimentology* **1966**, *6*, 73–93. [CrossRef]
54. Alsina, J.M.; Cáceres, I.; Brocchini, M.; Baldock, T.E. An experimental study on sediment transport and bed evolution under different swash zone morphological conditions. *Coast. Eng.* **2012**, *68*, 31–43. [CrossRef]
55. Cáceres-Euse, A.; Variano, E.A.; Toro-Botero, F.M.; Gómez-Giraldo, A.; Osorio, A.F. Simplified Model for Oscillatory Flow-Submerged Canopy Interaction. *J. Hydraul. Eng.* **2020**, *146*, 04020073. [CrossRef]
56. Gómez-Pujol, L.; Orfila, A.; Álvarez-Ellacuría, A.; Terrados, J.; Tintoré, J. Posidonia oceanica beach-cast litter in Mediterranean beaches: A coastal videomonitoring study. *J. Coast. Res.* **2013**, *165*, 1768–1773. [CrossRef]
57. Lowe, R.J.; Koseff, J.R.; Monismith, S.G. Oscillatory flow through submerged canopies: 1. Velocity structure. *J. Geophys. Res. Oceans* **2005**, *110*, 1–17. [CrossRef]
58. Van der A, D.A.; van der Zanden, J.; O'Donoghue, T.; Hurther, D.; Cáceres, I.; McLelland, S.J.; Ribberink, J.S. Large-scale laboratory study of breaking wave hydrodynamics over a fixed bar. *J. Geophys. Res. Ocean.* **2017**, *122*, 3287–3310. [CrossRef]
59. Elgar, S.; Guza, R.T.; Freilich, M.H. Eulerian measurements of horizontal accelerations in shoaling gravity waves. *J. Geophys. Res.* **1988**, *93*, 9261–9269. [CrossRef]
60. Goring, D.G.; Nikora, V.I. Despiking Acoustic Doppler Velocimeter Data. *J. Hydraul. Eng.* **2002**, *128*, 117–126. [CrossRef]
61. Cáceres, I.; Sánchez-Arcilla, A. Erosive and Accretive Mobile Bed Experiments in Large Scale Tests. In Proceedings of the Coastal Sediments 2015, San Diego, CA, USA, 11–15 May 2015. [CrossRef]
62. Van der A, D.A.; Ribberink, J.S.; van der Werf, J.J.; O'Donoghue, T.; Buijsrogge, R.H.; Kranenburg, W.M. Practical sand transport formula for non-breaking waves and currents. *Coast. Eng.* **2013**, *76*, 26–42. [CrossRef]
63. Luhar, M.; Coutu, S.; Infantes, E.; Fox, S.; Nepf, H. Wave-induced velocities inside a model seagrass bed. *J. Geophys. Res. Ocean.* **2010**, *115*, 1–15. [CrossRef]
64. Zhang, Y.; Tang, C.; Nepf, H. Turbulent Kinetic Energy in Submerged Model Canopies Under Oscillatory Flow. *Water Resour. Res.* **2018**, *54*, 1734–1750. [CrossRef]
65. Khorsandi, B.; Mydlarski, L.; Gaskin, S. Noise in Turbulence Measurements Using Acoustic Doppler Velocimetry. *J. Hydraul. Eng.* **2012**, *138*, 829–838. [CrossRef]
66. Grasso, F.; Michallet, H.; Barthélemy, E. Sediment transport associated with morphological beach changes forced by irregular asymmetric, skewed waves. *J. Geophys. Res.* **2011**, *116*, C03020. [CrossRef]
67. Grossmann, F.; Hurther, D.; van der Zanden, J.; Sánchez-Arcilla, A.; Alsina, J.M. Near-Bed Sediment Transport Processes During Onshore Bar Migration in Large-Scale Experiments: Comparison with Offshore Bar Migration. *J. Geophys. Res. Oceans* **2023**, *128*, e2022JC018998. [CrossRef]

68. Van der A, D.A.; O'Donoghue, T.; Ribberink, J.S. Measurements of sheet flow transport in acceleration-skewed oscillatory flow and comparison with practical formulations. *Coast. Eng.* **2010**, *57*, 331–342. [CrossRef]
69. Pan, Y.; Qu, X.; Yang, Y.; Zhang, J.; Wang, G.; Yin, S.; Chen, Y. Laboratory experiments on the evolution of a submerged berm driven by low-energy irregular waves. *Coast. Eng.* **2023**, *182*, 104301. [CrossRef]